IEEE Open Journal of the
Industrial Electronics Society

Received 12 August 2025; revised 17 September 2025; accepted 29 September 2025. Date of publication 3 October 2025;
date of current version 16 October 2025. The review of this article was arranged by Associate Editor Lefei Ge.

Digital Object Identifier 10.1109/OJIES.2025.3617573

Robust Decentralized PI Controller Design for Permanent Magnet Synchronous Generator

ADITYA KUMAR [1] (Student Member, IEEE), SHIV PRAKASH[1], SANDIP GHOSH [1] (Member, IEEE), N. K. SWAMI NAIDU [1], AND PAWEL DWORAK [2] (Senior Member, IEEE)

[1]Department of Electrical Engineering, Indian Institute of Technology (Banaras Hindu University), Varanasi 221005, India
[2]Department of Automatic Control and Robotics, West Pomeranian University of Technology in Szczecin, 70-310 Szczecin, Poland

CORRESPONDING AUTHOR: PAWEL DWORAK (e-mail: pawel.dworak@zut.edu.pl)

This work was supported in part by the Science, Engineering and Research Board (SERB), India, and in part by the Core Research under Grant CRG/2018/004481.

ABSTRACT This article considers the problem of controller design for a grid-connected wind energy conversion system (WECS) employing a variable-speed permanent magnet synchronous generator (PMSG). The system architecture comprises of two back-to-back converters connecting the PMSG to the grid. The variable-speed control of the PMSG using the machine-side converter employs a multi-input multioutput (MIMO) inner-loop current control. Although there are sophisticated control strategies to address MIMO design requirements, their practical deployment is often hindered by implementation complexity and computational demands for higher order controllers. In contrast, conventional proportional–integral (PI) controllers remain attractive for embedded applications because of their simplicity and easy hardware realizability. However, traditional PI control approaches rely on current-loop decoupling through feedforward compensation and thereby design in the single-input single-output framework, leading to suboptimal performances. To overcome this, a MIMO control design framework is proposed that explicitly considers the coupling in the system model. The controller design employs a two-stage approach: 1) designing the decentralized inner-loop current controllers in a MIMO framework and then 2) the outer-loop speed controller design. The structured PI controller requires the controller to be designed in a static output feedback framework. Simple weight functions in H_∞ robust control framework are chosen for the current-loop controller design to simplify the output feedback design criterion. While achieving robustness to disturbance rejection, the simultaneous regional pole placement criterion is used to ensure well-damped transient responses. Experiments on a laboratory-scale PMSG-based WECS validate the effectiveness of the proposed control design method that outperforms conventionally designed PI controllers in both transient and steady-state performances.

INDEX TERMS Permanent magnet synchronous generator (PMSG), proportional–integral (PI) control, H_∞ control.

NOMENCLATURE

Acronyms

DOBC	Disturbance observer-based control.
DTC	Direct torque control.
FCS-MPC	Finite control set model predictive control.
GM	Gain margin.
GSC	Grid-side converter.
IGBT	Insulated gate bipolar transistor.
LMI	Linear matrix inequality.
MPC	Model predictive control.
MPPT	Maximum power point tracking.
MSC	Machine-side converter.
PI	Proportional–integral.
PIDO	PI with disturbance observer.
PM	Phase margin.
PMSG	Permanent magnet synchronous generator.
PPR	Pulses per revolution.
PWM	Pulsewidth modulation.
RCPI	Robust centralized PI.
RDPI	Robust decentralized PI.
SMC	Sliding mode control.
SOF	Static output feedback.

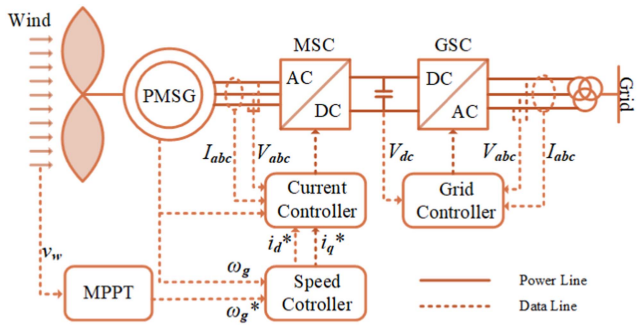

FIGURE 1. Block diagram of variable-speed PMSG-based WECS with grid connection through full-bridge converters.

VSC	Voltage source converter.
WECS	Wind energy conversion system.

Symbols

Γ_e, Γ_m	Electrical torque and mechanical torque.
λ_{opt}	Optimal tip speed ratio.
ω_g, ψ, p	Generator speed, flux linkage, and pole pairs.
B_m, K_t, J	Friction constant, torque constant, and inertia.
C_p	Power coefficient.
e_d, e_q	i_d and i_q loop error signals.
I_{abcg}, V_{abcg}	Grid three-phase currents and voltages.
$i_{dg}, i_{qg}, v_{dg}, v_{qg}$	Grid d- and q-axis currents and voltages.
K_c, K_s	Current and speed controller gain matrices.
$k_{id}, k_{iq}, k_{i\omega}$	i_d, i_q, and speed loop integral gains.
$k_{pd}, k_{pq}, k_{p\omega}$	i_d, i_q, and speed loop proportional gains.
R, L	Generator stator resistance and inductance.
R_b	Wind turbine blade radius.
V_w	Wind speed.
i_d, i_q, v_d, v_q	Generator d- and q-axis currents and voltages.
I_{abcm}, V_{abcm}	Generator three-phase currents and voltages.

I. INTRODUCTION

A grid-connected WECS employing a variable-speed PMSG is illustrated in Fig. 1. The system architecture comprises a pmsg interfaced with the utility grid through two VSCs: the MSC and the GSC, interconnected via a common direct current (dc)-link. This back-to-back converter configuration enhances control flexibility and improves overall system performance [1]. PMSG-based WECSs are widely favoured over other power conversion technologies due to several benefits, including the elimination of gearboxes, which improves reliability, reduces mechanical complexity, and lowers maintenance requirements. In addition, their high power density makes them ideal for modern wind turbine applications.

Despite the advantages of enhanced control flexibility in variable-speed WECS, selecting and designing appropriate control strategies remains a significant challenge. Typically, maximum power extraction is achieved by regulating the generator speed through an outer-loop controller, while the MSC inner loop tracks the electromagnetic torque using dq-axis current vector control [2]. Meanwhile, the GSC regulates the dc-link voltage and ensures synchronized power injection into the grid, generally operating independently from the MSC [3]. A major difficulty in this configuration arises from the inherent coupling between the mechanical and electrical dynamics of the PMSG. The dq current control loops inherently form a MIMO system, which complicates controller design and tuning. In [4], a MIMO control methodology was adopted, resulting in a higher order controller with additional cross-coupling terms that further increase the implementation complexity.

PI controllers are widely adopted due to their simplicity, ease of implementation, and compatibility with embedded hardware. However, designing PI controllers for MIMO systems presents additional challenges. The conflicting performance requirements of the coupled dq control loops often necessitate decoupling techniques, such as feedforward compensators to approximate the system as a decoupled SISO system [5], [6]. This typically results in identical transfer functions and symmetric control gains in the dq frame. Nonetheless, these approximations rely on frequency-domain heuristics that link GM and PM to time-domain performance [7], potentially resulting in suboptimal dynamic behavior. Furthermore, such designs often lead to high integral gains. Although such high gains eliminate the steady-state error, they often lead to actuator saturation. It may be noted that actuator saturation results in extreme operation of the actuators and loss of dynamic control performance. The problem of actuator saturation often necessitates employing antiwindup mechanisms [8], [9].

Besides PI control, several nonlinear and predictive control techniques have been explored to address the intrinsic complexity and uncertainties in WECS. DTC offers fast torque response and simplicity but suffers from high torque and flux ripples due to variable switching frequency. Backstepping control [10], [11], based on Lyapunov theory, provides robustness and adaptability, but its recursive design process and structural limitations complicate its application to higherorder systems. Attempts to reduce its computational burden, such as command-filtered backstepping, dynamic surface control, and neuro-adaptive techniques are also discussed in the literature [12], [13].

MPC, particularly its FCS-MPC formulation, offers excellent dynamic performance by evaluating all feasible switching states to minimize a predefined cost function online [14], [15], [16]. Despite its advantages, FCS-MPC is highly sensitive to model mismatches and imposes significant computational demands, which limit its practicality for embedded applications. Similarly, SMC [17], [18] and DOBC have been extensively studied for their robustness against system uncertainties. Especially, the DOBC combined with feedback linearization seeks to restore nominal system dynamics under disturbances by employing high-gain and/or reduced-order observers. Recent works also explored the SMC relying on

passivity-based control using interconnection and damping assignment with the controller parameters optimized using heuristic genetic algorithm [19], [20].

Based on these ideas, PI controllers is represented in the DOBC framework [21] to enhance both the transient and steady-state performances. While this approach improves disturbance rejection and response quality, actuator saturation remains a concern that is addressed using antiwindup compensators. A hybrid control scheme is also proposed in [21] that combines PI control with SMC, offering a balance between simplicity of implementation and robustness. Despite the advantages in performance, their real-time implementation is hindered by computational overhead, modeling complexity, and hardware constraints. Consequently, improving conventional PI control in MIMO systems remains an attractive solution due to its simplicity and easy compatibility to embedded platforms.

In light of these practical constraints and performance tradeoffs, this article focuses on enhancing PI controller design for PMSG-based WECS by retaining the MIMO system structure while addressing its limitations. The main contributions are as follows.

1) Formulating the PI current controller (without the conventional decoupling controller) design as a decentralized SOF controller design problem, retaining the coupling of the two control loops in the system dynamics.
2) Defining system performance in the H_∞ control framework for disturbance rejection and incorporating a regional pole-placement criterion to ensure well-damped transient response.
3) Utilizing a new novel yet straightforward LMI-based criterion for designing the current controllers using simple weight functions.
4) Employing the same output feedback framework to design the speed-loop PI controller.

The proposed controller design is validated experimentally on a laboratory-scale PMSG-based WECS setup, achieving improved transient and steady-state performances compared to conventional PI controllers.

II. MACHINE DYNAMICS AND CONTROL STRATEGY

The dynamical model of a surface-mounted PMSG in the synchronously rotating dq-reference frame, aligned with the rotor magnetic flux, can be expressed as follows [22]:

$$\frac{di_d}{dt} = -\frac{R}{L}i_d + p\omega_g i_q + \frac{1}{L}v_d \tag{1a}$$

$$\frac{di_q}{dt} = -\frac{R}{L}i_q - p\omega_g i_d - \frac{p\omega_g \psi}{L} + \frac{1}{L}v_q \tag{1b}$$

$$\frac{d\omega_g}{dt} = \frac{\Gamma_m}{J} - \frac{K_t i_q}{J} - \frac{B_m \omega_g}{J}. \tag{1c}$$

The machine-side control strategy for the system in Fig. 1 is depicted in Fig. 2. The cascaded control strategy has two nested loops as the following.

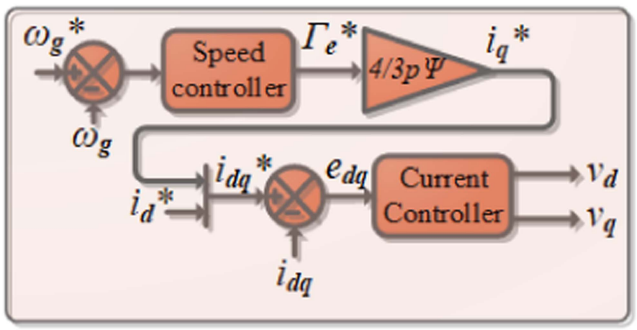

FIGURE 2. Cascaded control scheme with outer-loop speed controller generating reference for inner-loop current controllers.

- An outer-loop speed controller to track the reference speed ω_g^* to achieve MPPT under varying wind conditions.
- A pair of inner-loop current controllers to track the reference currents i_d^* and i_q^* to generate the corresponding voltage vectors v_d and v_q for the MSC.

The speed controller generates the torque reference Γ_e^*, which is transformed to i_q^* using the relation $i_q^* = \frac{\Gamma_e^*}{K_t}$, where $K_t = \frac{3p\psi}{4}$. The speed controller is slower due to the mechanical system's large time constant, primarily influenced by the wind turbine's significant inertia. In contrast, faster current control is essential for high-performance operation, minimizing harmonics and ensuring stator current balance. For unity power factor operation, the current reference i_d^* is set to 0 to improve efficiency by reducing resistive losses in the stator, that allows the current i_q to be maximized. However, in field-weakening mode, i_d^* may be nonzero to enable operation above the rated speed [22].

A. CURRENT CONTROL CONFIGURATIONS

This section further discusses possible configurations for the pair of current control loops. It can be categorized into three schemes as follows.

1) CONVENTIONAL PI CONTROL

In the conventional approach, shown in Fig. 3(a), feedforward compensating controls decouple the two current dynamics, enabling a simplified SISO design for the two PI (or its variants) controllers. The voltage demands for the MSC are obtained as [8]

$$v_d = k_{pd}e_d + k_{id}\int e_d dt - Lp\omega_g i_q^* \tag{2a}$$

$$v_q = k_{pq}e_q + k_{iq}\int e_q dt + Lp\omega_g i_d^* + p\omega_g \psi. \tag{2b}$$

The resulting transfer function for the compensated PMSG dynamics (1) simplifies to a first-order one as

$$G'_{dq}(s) = \frac{i_d(s)}{v_d(s)} = \frac{i_q(s)}{v_q(s)} = \frac{1}{R+Ls}. \tag{3}$$

This scheme simplifies controller design, as i_d and i_q share the same transfer function, allowing identical gains for both

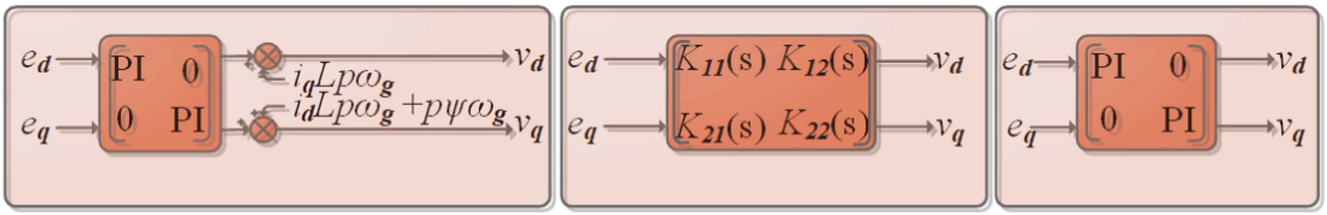

FIGURE 3. Current-loop control configurations. (a) PI control with feedforward decoupling. (b) Centralized control. (c) Decentralized PI control.

the loops. However, this approach often leads to suboptimal performance due to shared gain values.

2) CENTRALIZED CONTROL

The centralized control scheme, shown in Fig. 3(b), eliminates compensating terms and employs a unified MIMO design approach. For instance, an H_∞ robust controller is designed in [4] to independently regulate the reactive power (i_d) and generator speed (ω_g). While this approach is flexible and supports a range of design objectives, the absence of integrators in the controller structure compromises steady-state performance. In addition, coupling between current loops and the complexity of high-order controllers pose implementation challenges. A PI controller structure for the centralized approach can also be considered, as discussed later in this work.

3) DECENTRALIZED PI CONTROL

Decentralized PI control, shown in Fig. 3(c), represents the simplest configuration but faces significant challenges due to 1) MIMO control setup and 2) restricted controller structure.

This work employs a robust control design approach to design such decentralized PI controllers overcoming the above-mentioned challenges. The proposed design provides an effective alternative to the conventional approaches.

III. ROBUST DECENTRALIZED PI CONTROL DESIGN

The design of the current controller and speed controllers is presented in this section. The controllers are designed in two sequential steps: 1) First, the current controllers are designed considering the machine dynamics, and 2) the speed controller is designed. Hence, the speed controller is dependent on the current controller gains. This is a conventional approach for the design, and the same is followed here.

A. CURRENT CONTROL DESIGN FORMULATION

The two outputs of the current-loop PI controllers are

$$v_d = k_{pd} e_d + k_{id} \int e_d \, dt \tag{4a}$$

$$v_q = k_{pq} e_q + k_{iq} \int e_q \, dt. \tag{4b}$$

Defining the states as $x_c = \begin{bmatrix} x_1 & x_2 & x_3 & x_4 \end{bmatrix}^T$ with $x_1 = (i_d^* - i_d)$, $x_2 = (i_q^* - i_q)$, $x_3 = \int (i_d^* - i_d)\, dt$, and $x_4 = \int (i_q^* - i_q)\, dt$, the current dynamics (1a) and (1b) along with (4) at a reference speed ω_g^* can be written as

$$\dot{x}_c = (A_c + B_c K_c C_c) x_c + B_{c\mathbf{w}} \mathbf{w}_c \tag{5}$$

where $\mathbf{w}_c = \omega_g$ and

$$A_c = \begin{bmatrix} -\frac{R}{L} & p\omega_g^* & 0 & 0 \\ -p\omega_g^* & -\frac{R}{L} & 0 & 0 \\ 1 & 0 & 0 & 0 \\ 0 & 1 & 0 & 0 \end{bmatrix}, \quad B_c = \begin{bmatrix} -\frac{1}{L} & 0 \\ 0 & -\frac{1}{L} \\ 0 & 0 \\ 0 & 0 \end{bmatrix}$$

$$C_c = \begin{bmatrix} 1 & 0 & 0 & 0 \\ 0 & 0 & 1 & 0 \\ 0 & 1 & 0 & 0 \\ 0 & 0 & 0 & 1 \end{bmatrix}, \quad K_c = \begin{bmatrix} k_{pd} & k_{id} & 0 & 0 \\ 0 & 0 & k_{pq} & k_{iq} \end{bmatrix}$$

$$B_{c\mathbf{w}} = \begin{bmatrix} 0 & \frac{p\psi}{L} & 0 & 0 \end{bmatrix}.$$

Note that the control gain K_c contains the PI controller parameters to be designed. Also, K_c is in decentralized form and requires output feedback control design methods to be adopted, contrary to a centralized one for which K_c is a full matrix, which conforms to the structure in Fig. 3(b) with each element having a PI structure.

B. SPEED CONTROL DESIGN FORMULATION

The output of the speed controller can be written as

$$\Gamma_e^* = k_{p\omega} e_\omega + k_{i\omega} \int (\omega_g^* - \omega_g)\, dt. \tag{6}$$

Considering that the current controller has already been designed, the overall system dynamics at a speed operating point ω_g^* can be represented as

$$\dot{x}_s = (A_s + B_s K_s C_s) x_s + B_{s\mathbf{w}} \mathbf{w}_g \tag{7}$$

where $x_s = \begin{bmatrix} x_c^T & x_5 & x_6 \end{bmatrix}^T$ with $x_5 = (\omega_g^* - \omega_g)$ and $x_6 = \int (\omega_g^* - \omega_g)\, dt$

$$A_s = \begin{bmatrix} -\Sigma_1 & p\omega_g^* & -\frac{k_{id}}{L} & 0 & -\Sigma_3 & 0 \\ -p\omega_g^* & \Sigma_2 & 0 & -\frac{k_{iq}}{L} & -\frac{p\psi}{L} & 0 \\ 1 & 0 & 0 & 0 & 0 & 0 \\ 0 & 1 & 0 & 0 & 0 & 0 \\ 0 & -\frac{k_t}{J} & 0 & 0 & -\frac{B_m}{J} & 0 \\ 0 & 0 & 0 & 0 & 1 & 0 \end{bmatrix}$$

$$B_s = \begin{bmatrix} 0 & -\frac{R}{Lk_t} & 0 & 0 & \frac{1}{J} & 0 \end{bmatrix}^T, \quad K_s = \begin{bmatrix} k_{p\omega} & k_{i\omega} \end{bmatrix}$$

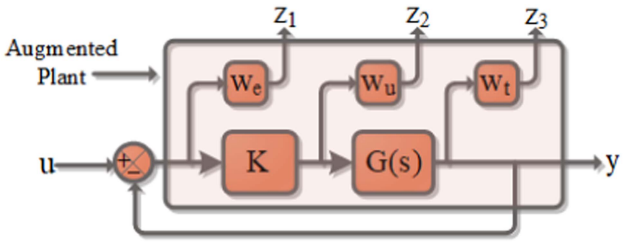

FIGURE 4. Augmented system with weights on the error signal, control input, and system output as $\mathbf{w}_e$, $\mathbf{w}_u$, and $\mathbf{w}_t$, respectively.

$$C_s = \begin{bmatrix} 0 & 0 & 0 & 0 & 1 & 0 \\ 0 & 0 & 0 & 0 & 0 & 1 \end{bmatrix}, \quad \mathbf{w}_s = \Gamma_m$$

$$B_{s\mathbf{w}} = \begin{bmatrix} 0 & 0 & 0 & 0 & \frac{1}{J} & 0 \end{bmatrix}^T$$

with $\Sigma_1 = \frac{R}{L} - \frac{k_{pd}}{L}$, $\Sigma_2 = -\frac{R}{L} - \frac{k_{pq}}{L}$, and $\Sigma_3 = \frac{p(\Gamma_m - B_m\omega_g^*)}{K_t}$. The requirement is now to design K_s that contains the speed controller gains.

C. CONTROL DESIGN METHOD

The design of the above-mentioned controllers can be carried out in an SOF framework. In the first case, in (5), though it appears to be a state feedback controller design (number of states and output are equal), the restricted nature of the feedback enforces it to be an SOF problem. In the second case, the SOF problem is straightforward in (7), though no feedback restriction is there. Designing SOF controllers is challenging and often solved using sufficient conditions in a robust control design framework. Such designs also facilitate centralized and decentralized feedback structure, which is the requirement here.

In order to attain robust performance while implicitly accounting for voltage and current constraints, the robust control design framework for the plant $G(s)$ and its controller K, as shown in Fig. 4, incorporates appropriately selected weight functions W_e, W_u, and W_t [23]. These weight functions shape the closed-loop behavior by balancing performance, robustness, and control effort.

1) *Error Weight (W_e):* It penalizes the tracking error. A low-pass filter is chosen so that weight on tracking error at low frequency is high. Note that, out of the two current-loops, the i_d-loop requires less aggressive control, whereas the i_q loop demands tighter tracking to satisfy torque requirements.
2) *Control Input Weight (W_u):* It penalizes excessive control effort. Differentiated weights for the two current-loops, such as, $W_u = \text{diag}(0.15, 0.1)$, prioritize smoother control for the i_d-loop while allowing more aggressive control for the i_q loop.
3) *System Output Weight (W_t):* A high-pass filter weight, such as $W_t = \frac{s}{s+\omega_{hc}}$ (with $\omega_{hc} = 1000$) leads to high-frequency disturbance/noise rejection, which is invariably desired in electrical machine drives applications.

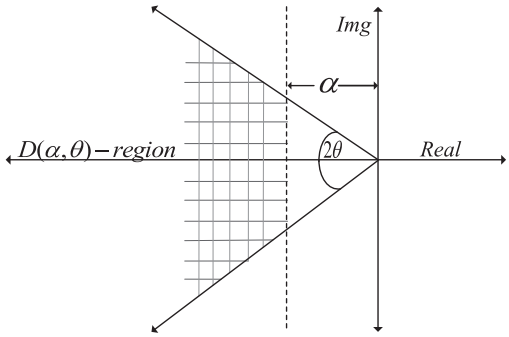

FIGURE 5. Pole placement region for ensuring transient performance.

Remark III.1: As appropriate selection of W_t is concerned to account for nonidealities and uncertainties in the system, such as magnetic saturation and temperature effects that lead to the system parameters R and L to be uncertain [24]. Although appropriate modeling of such uncertainties was not carried out in this article, the consideration of W_t enforces that the design is robust to some extent with respect to such uncertain variations.

These weight functions help shape the control response while trading-off the different performances with the control input.

A generic representation of the control problem with augmented weight functions with the plant model in the form of (4) or (7) is given as

$$\dot{x}(t) = Ax(t) + Bu(t) + B_{\mathbf{w}}\mathbf{w}(t) \tag{8a}$$

$$z(t) = C_z x(t) + D_{zu}u(t), \quad y(t) = Cx(t) \tag{8b}$$

where $x(t) \in \mathbb{R}^n$ and $u(t) \in \mathbb{R}^m$ are the state of the weight-augmented plant and its control input, respectively. $z(t) \in \mathbb{R}^{p_1}$ and $y(t) \in \mathbb{R}^p$ are the controlled and measured output, respectively, and $\mathbf{w}(t) \in \mathbb{R}^{m_1}$ is the disturbance input. A, B, C, $B_{\mathbf{w}}$, C_z, and D_{zu} are matrices of appropriate dimensions. For the SOF controller $u(t) = Ky(t)$ ($K = K_c$ or $K = K_s$ as the case is), the closed-loop transfer function from the disturbance input $\mathbf{w}(t)$ to the controlled output $z(t)$ is

$$T_{z\mathbf{w}}(s) = C_z\,(sI - (A + BKC))^{-1}\,B_{\mathbf{w}}. \tag{9}$$

The objective is to design the feedback controller gain K that:

1) minimizes $\|T_{z\mathbf{w}}\|_\infty$ to reduce the effect of $\mathbf{w}(t)$;
2) ensures transient performance in terms of minimum decay rate α and damping ratio $\xi = \cos(\theta)$ through regional pole placement [25] in the $D(\alpha, \theta)$-region (the shaded area as shown in Fig. 5).

Such a problem is solved using LMI synthesis criteria in a multiobjective framework [26]. However, it is well known that the synthesis of SOF controllers (controllers with a specified structure other than the centralized one) is NP-hard [27]. One way to tackle this is by approximating the nonlinear matrix term $BKCX$ in the quadratic analysis so that the resulting criterion becomes an LMI [28]. Out of the several such approximations, one is by using a decomposition of X exploiting the null-space and range-space of the C matrix.

However, such solutions involve choosing a few scalar parameters beforehand for solving LMIs. While the result of [28] can be directly applied to speed controller design, for constant weight functions, it can be simplified (particularly relaxing the requirement of choosing scalar parameters beforehand) for the current-loop controller design since the numbers of the outputs and states are equal (C has full row-rank. This simplified result is provided in the next section along with the SOF design criteion of [28] both of which are used in this work for controller design.

1) CURRENT CONTROLLER DESIGN CRITERIA

The following results provide the two LMI-based controller synthesis criteria for the two design objectives.

Theorem 1 (H_∞ performance criterion): For MIMO plants with full row-rank output matrices, the system (8) is stable with the SOF controller, and performance $\|T_{z\mathbf{w}}\|_\infty < \gamma$ is guaranteed if there exists $X_R = X_R^T > 0$ and Y_C satisfying the following LMI (with $*$ represents the symmetric components):

$$\begin{bmatrix} \mathrm{Sym}\{AR_cX_RR_c^T + BY_cR_c^T\} & * & * \\ B_{\mathbf{w}}^T & -\gamma^2 I & * \\ C_zR_cX_RR_c^T + D_{zu}Y_cR_c^T & 0 & -I \end{bmatrix} < 0. \quad (10)$$

Proof: Following the bounded real lemma [29], we can write that $\|T_{z\mathbf{w}}\|_\infty < \gamma$ and $A + BKC$ is Hurwitz if there exists $X = X^T > 0$ satisfying the following condition:

$$\begin{bmatrix} \mathrm{Sym}\{A_{cl}X\} & * & * \\ B_{cl}^T & -\gamma^2 I & * \\ C_{cl}X & 0 & -I \end{bmatrix} < 0 \quad (11)$$

where, $A_{cl} = A + BKC$, $B_{cl} = B_{\mathbf{w}}^T$, $C_{cl} = C_z + D_{zu}KC$. Since C is full-rank, consider $R_c = C^{-1}$ so that $CR_c = I$ and a decomposition of X as

$$X = R_cX_RR_c^T. \quad (12)$$

Note that $X_R > 0$ ensures $X > 0$. Now, substituting (12) into (11), one obtains Theorem 1 by replacing

$$KX_R = Y_c. \quad (13)$$

Theorem 2 (Pole-placement criterion): For MIMO plants with full row-rank output matrices, the closed-loop poles of the system (8) are placed in the region $D(\alpha, \theta)$ if there exists $X_R = X_R^T > 0$ satisfying the following LMIs:

$$\begin{bmatrix} s_\theta\left(\mathrm{Sym}\{\Xi_1 + \Xi_2\}\right) & * \\ c_\theta\left(\Xi_1^T + \Xi_2^T - \Xi_1 - \Xi_2\right) & s_\theta\left(\mathrm{Sym}\{\Xi_1\}\right) \end{bmatrix} < 0 \quad (14a)$$

$$\mathrm{Sym}\{\Xi_1 + \Xi_2\} + 2\alpha R_cX_RR_c^T < 0 \quad (14b)$$

where $s_\theta = \sin\theta$, $c_\theta = \cos\theta$, $\Xi_1 = AR_cX_RR_c^T$, $\Xi_2 = BY_cR_c^T$.

Proof: Following [25], the criterion for closed-loop poles to be in $D(\alpha, \theta)$ is as follows:

$$\begin{bmatrix} s_\theta(\mathrm{Sym}\{A_{cl}X\}) & * \\ c_\theta(XA_{cl}^T - A_{cl}X) & s_\theta(\mathrm{Sym}\{A_{cl}X\}) \end{bmatrix} < 0 \quad (15a)$$

$$\mathrm{Sym}\{A_{cl}X\} + 2\alpha X < 0 \quad (15b)$$

$$X > 0. \quad (15c)$$

The first condition (15a) ensures the poles of A_{cl} are in the conic sector with angle 2θ and apex at the origin, as shown in Fig. 5. The second condition (15b) ensures the poles are in the left-half plane to the right of the vertical line through $(-\alpha, 0)$. Substituting (12) into (15) and incorporating (13) results in (14).

Solving the LMIs (10) and (14) simultaneously with the same X_R, R_c, and Y_c yields the controller gain K as in (13) that satisfy both the design objectives. For a decentralized controller structure of K [for K_c in (4)], X_R is to be chosen as a diagonal matrix and Y_c should have the same structural entries as the K so that solving (13) yields the particular structured SOF controller. If X_R and Y_c are full matrices, the resultant K becomes centralized. The centralized and decentralized designs are later made in Section IV.

2) SPEED CONTROL DESIGN METHOD

Since the C matrix is not of full rank for the speed controller corresponding to (7), the result of [28] is used here. For completeness, the result is recalled in the following.

Consider $R_c \in \mathcal{R}(C)$ and $Q_c \in \mathcal{N}(C)$ with $\mathcal{R}(C)$ and $\mathcal{N}(C)$ represent the range-space and null-space of C, respectively, so that $CR_c = I$ and $CQ_c = 0$. Then, $X > 0$ is decomposed as $X = \begin{bmatrix} Q_c^T \\ R_c^T \end{bmatrix}^T \begin{bmatrix} X_Q & X_s \\ X_s^T & X_R \end{bmatrix} \begin{bmatrix} Q_c^T \\ R_c^T \end{bmatrix}$ with $\begin{bmatrix} X_Q & X_s \\ X_s^T & X_R \end{bmatrix} > 0$. Also, consider the change of variable (13).

Theorem 3 (H_∞ performance criterion [28]): The system (8) with the SOF controller is stable with guaranteed performance $\|T_{z\mathbf{w}}\| < \gamma$ if, for scalars ρ_1 and ρ_2, there exist $X_Q = X_Q^T$, $X_R = X_R^T$, $Z_R = Z_R^T$, X_s, and Y_c satisfying the following LMIs:

$$\begin{bmatrix} \Psi_1 & * & * & * & * \\ \Psi_2 & -\gamma^2 I & * & * & * \\ \Psi_3 & D_{z\mathbf{w}} & -I & * & * \\ \Psi_4^T & 0 & Y_c^T D_{zu}^T & -Z_R & * \\ \rho X_S^T Q_C^T & \rho_1 D_{z\mathbf{w}} & 0 & 0 & -\Psi_5 \end{bmatrix} < 0 \quad (16a)$$

$$\begin{bmatrix} X_Q & X_s \\ X_s^T & X_R \end{bmatrix} > 0 \quad (16b)$$

where $\Psi_1 = \mathrm{Sym}\{\Xi_3 + \Xi_4\}$, $\Xi_3 = AX$, $X = Q_cX_QQ_c^T + Q_cX_sR_c^T + R_cX_s^TQ_c^T + R_cX_RR_c^T$, $\Xi_4 = BY_cR_c^T - \rho_2R_cX_S^TQ_c^T$, $\Psi_2 = B_{\mathbf{w}}^T - \rho_2R_cX_s^TQ_c^T$, $\Psi_3 = C_zX + D_{zu}Y_cR_c^T$, $\Psi_4 = BY_c + \rho_2R_cX_R$, $\Psi_5 = \mathrm{Sym}\{\rho_1X_R\} - Z_R$.

Theorem 4 (Pole-placement criterion [28]): Closed-loop poles of system (8) are placed in the region $D(\alpha, \theta)$ if, for scalars β_1 and β_2, there exists $X_Q = X_Q^T$, $X_R = X_R^T$, $Z_{R1} = Z_{R1}^T > 0$, $Z_{R2} = Z_{R2}^T > 0$, X_s, and Y_c satisfying the following

LMIs:

$$\begin{bmatrix} s_\theta\Psi_1 & * & * & * & * & * \\ c_\theta\Psi_6 & s_\theta\Psi_1 & * & * & * & * \\ s_\theta\Psi_4^T & -c_\theta\Psi_4^T & -Z_{R1} & * & * & * \\ c_\theta\Psi_4^T & s_\theta\Psi_4^T & 0 & -Z_{R1} & * & * \\ \beta_1\Pi_1^T & 0 & 0 & 0 & -\Pi_2 & * \\ 0 & \beta_2\Pi_1^T & 0 & 0 & 0 & -\Pi_2 \end{bmatrix} < 0 \tag{17a}$$

$$\mathrm{Sym}\{\Xi_3 + \Xi_4\} + 2\alpha R_c X_R R_c^T < 0 \tag{17b}$$

where $\Psi_6 = \Xi_3^T - \Xi_3 + \Xi_4^T - \Xi_4$, $\Pi_1 = Q_c X_s$, $\Pi_2 = \mathrm{Sym}\{\beta_1 X_R\} - Z_{R1}$, $\Pi_3 = \mathrm{Sym}\{\beta_2 X_R\} - Z_{R2}$; Ψ_1, Ψ_4, Ξ_3, and Ξ_4 are as defined earlier in (16).

Note that above-mentioned Theorem 4 is slightly different from Theorem 3 in [28] in the way that the conditions here are derived as per the pole-placement condition (15).

Similar to the current controller design, both (16) and (17) with the same LMI variables X and Y_c are solved together to obtain the speed controller. This work uses the scalar parameters as $\rho_1 = \rho_2 = \beta_1 = \beta_2 = 1$ to simplify the design. One may fine-tune these parameters for further improvements in the design.

D. CONTROLLER DESIGN STEPS

The controller design procedure using the SOF framework for both the current and speed loops is summarized as follows. The steps indicate where the design methodology differs for the two cases.

1) *Plant Augmentation:* Augment the plant $G(s)$ with appropriate weighting functions W_e, W_u, and W_t to capture performance, robustness, and control effort tradeoffs, as shown in Fig. 4.
2) *State–Space Formulation:* Represent the augmented plant in the standard form of (8), defining:
   a) $\mathbf{w}(t)$ as the disturbance input;
   b) $y(t)$ as the measured output;
   c) $z(t)$ as the controlled output.
3) *Controller Structure Selection:*
   - *Centralized SOF:* Full controller gain K with no structural constraints.
   - *Decentralized SOF:* Diagonal X_R and structured Y_c matching the desired sparsity of K.
4) *Define Design Objectives:*
   a) Minimize $\|T_{z\mathbf{w}}\|_\infty$ to ensure disturbance rejection and robustness.
   b) Ensure desired transient performance by placing closed-loop poles in the $D(\alpha, \theta)$ region (see Fig. 5).
5) *LMI Formulation:*
   - *For current loop design (full-rank C matrix):* Use the simplified results given in Theorems 1 and 2, where the decomposition $X = R_c X_R R_c^T$ is valid since C is full row-rank.
   - *For speed loop design (non-full-rank C matrix):* Use the generalized results of [28] as recalled in Theorems 3 and 4, where X is decomposed using range-space $R_c \in \mathcal{R}(C)$ and null-space $Q_c \in \mathcal{N}(C)$

$$X = \begin{bmatrix} Q_c & R_c \end{bmatrix} \begin{bmatrix} X_Q & X_s \\ X_s^T & X_R \end{bmatrix} \begin{bmatrix} Q_c^T \\ R_c^T \end{bmatrix}.$$

     This step introduces additional scalar parameters $(\rho_1, \rho_2, \beta_1, \beta_2)$ and auxiliary variables (Z_R, Z_{R1}, Z_{R2}).
6) *Simultaneous Multiobjective Solution:* Solve both LMIs together.
   - For current loop: LMIs in (10) and (14).
   - For speed loop: LMIs in (16) and (17). This ensures that both H_∞ performance and regional pole placement objectives are satisfied simultaneously.
7) *Compute Controller Gain:* Recover the controller gain using

$$K = Y_c X_R^{-1}.$$

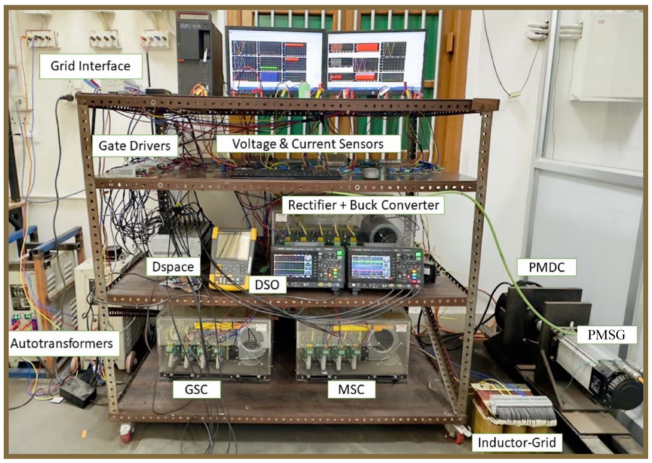

FIGURE 6. Experimental setup for the grid-connected PMSG wecs.

IV. EXPERIMENTAL RESULTS

A. EXPERIMENTAL SETUP

The experimental setup is shown in Fig. 6. An eight-pole 5 HP PMSG (Infranor Mavilor make) is used to validate the proposed control design method. The MSC and GSC are identical three-phase VSCs with six IGBT switches connected back-to-back with a bank of two 4700 μF dc-link capacitors to absorb high-frequency transients. An autotransformer through a series 5 mH L-filter connects the GSC to the grid. An incremental encoder of 1000 ppr is used to measure the angle and speed of the PMSG. Appropriate Hall-effect sensors (LEM make) are used for current and voltage measurements.

The PMSG is driven by a 4.2 kW dc motor that emulates a wind turbine. A buck chopper powers the dc motor through a 2.1 mH inductor and a 470 μF capacitor filter. A three-phase diode bridge rectifier provides the dc input to the buck chopper from the grid.

A dSPACE MicroLabBox (DS1102) with inbuilt analog and digital I/O channels and 50 μs sample time is used to implement the controller and to generate the PWM signals for the VSCs and buck chopper through optocouplers. The GSC and MSC are switched at 10 kHz, while the buck chopper is switched at 20 kHz. For digital implementation, the continuous-time PI controllers are transformed into the discrete domain using the Tustin transformation given by

$$s \approx \frac{2}{T_s} \cdot \frac{1 - z^{-1}}{1 + z^{-1}}. \tag{18}$$

Then, the discrete-time PI controller is obtained as

$$G(z) = K_p + K_i \frac{T_s}{2} \frac{1 + z^{-1}}{1 - z^{-1}}. \tag{19}$$

A smaller sampling time with respect to the PWM frequency ensures performance achievement with the designed controller [30], [31].

A conventional PI controller [3] is used for the GSC to maintain the dc-link voltage at 175 V while the grid voltage is set at 60 V. The PI controller is designed following [3] to reject external disturbances and recover nominal performance in the steady state.

Two experimental situations are considered for emulating the wind turbine in the dc machine.

1) Constant speed mode: This mode is used for validating the performance of the inner current-loop controllers.
2) Constant power mode: This mode evaluates the overall system's performance, where both the current and speed controllers are used.

B. DESIGN COMPARISON OF CURRENT CONTROLLERS

The performance of the designed current controller is compared with two conventional PI [9], [32] with disturbance observer (PIDO) of [33] designs. The above-mentioned PI designs include feedforward compensators. The RDPI controller design is also compared with a centralized controller (RCPI) design in the same framework.

1) EXISTING PI DESIGN [9] (DENOTED AS PI-1)

The design is based on selecting a suitable open-loop bandwidth of the SISO system. The open-loop bandwidth is determined as $\omega_{cc} = \frac{1}{1-\Delta}\frac{R}{L}$, where $\Delta \in [0, 1]$ is a normalising parameter chosen here as 0.9. The controller gains are then obtained as $k_p = L\omega_{cc}$ and $k_i = R\omega_{cc}$.

2) EXISTING PI DESIGN [32] (DENOTED AS PI-2)

It is based on the pole-placement design of a nominal plant considering exact feedforward compensation. By comparing the parameterized closed-loop characteristic polynomial with a desired one, the controller gains are obtained as $k_p = 2\xi\omega_{cc}L - R$ and $k_i = \frac{k_p}{\tau_i}$ with $\tau_i = \frac{2\xi\omega_{cc}L - R}{L\omega_{cc}^2}$, where ω_{cc} is as defined in the previous method, and the damping factor ξ is chosen as 0.7.

TABLE 1. Designed Current Controller Gains

Gains	RDPI	PI-1 [9]	PI-2 [32]	PIDO [33]
k_{pd}	6.5	6.3	8.26	7.7
k_{id}	2130	1469	14696	5000
k_{pq}	11.1	6.3	8.26	10.7
k_{iq}	4058	1469	14696	8000
The four PI controller gains of RCPI				
	i_d	i_q	$i_d - i_q$	$i_q - i_d$
k_p	4.4	8.2	0.1	0
k_i	1166	2428	161	173

3) EXISTING PIDO DESIGN [33]

A DOBC is deduced to a decoupled PI controller with a reference jump and antiwindup compensators in [33]. Retaining the main features of the PI control, it is considered here for a comparison with other PI controller designs. The same notation as in (41) and (42) of [33] is used here to present the designed controller briefly as follows. A desired settling time of $t_s = 4$ ms is chosen that leads to $k_{d,q} = 0.25t_s^{-1}$. The gains l_d and l_q are selected as 5 and 8, respectively. Then, PI controller gains are obtained as $k_p = l_{d,q}k_{d,q} + L_{d,q}$ and $k_i = l_{d,q}k_{d,q}$.

4) RDPI DESIGN

The PI controllers are designed using the method in Section III, particularly using Theorem 1. First, appropriate weight functions (following Fig. 4) are chosen. The objectives of the two control loops for i_d and i_q are different. The i_d is regulated at zero and requires lesser control effort. Conversely, the i_q follows the speed demand, requiring comparatively tighter control effort to meet the tracking objective. Thus, the weight on the control input is chosen as $W_u = \text{diag}(0.15, 0.1)$ so that a relatively higher weight on v_d adjusts for the different control requirements. This leads to smaller i_d-loop gains, leading to lesser control effort. The error weight is chosen as $W_e = \text{diag}(0.1, 0.1)$. The pole placement criterion is also added to the design to ensure the transient performance of the closed-loop system. The parameters for the pole placement (see Fig. 5) are chosen as $\alpha = 100$ and $\phi = 50^\circ$, for the inner current loop. These values ensure that the current transients decay faster than e^{-100t}, with a minimum damping ratio of 0.643. The corresponding minimum response time is approximately $1/\alpha \approx 0.01$ s, which provides sufficiently fast and well-damped current dynamics relative to the slower speed loop. The RDPI controller design follows a MIMO design procedure retaining the coupling of both the loops (excluding the decoupling compensator) and yields tighter i_q-loop gain than the i_d-loop.

5) RCPI DESIGN

An RCPI controller has the structure as in Fig. 3(b), with all four controller transfer functions are PI ones. The RCPI is designed with the same weights as the RDPI controller with the variables Y_C and X_R in Theorem 1 taking their full matrix structure. The designed control gains using the above-mentioned methods are listed in Table 1. The RCPI controller

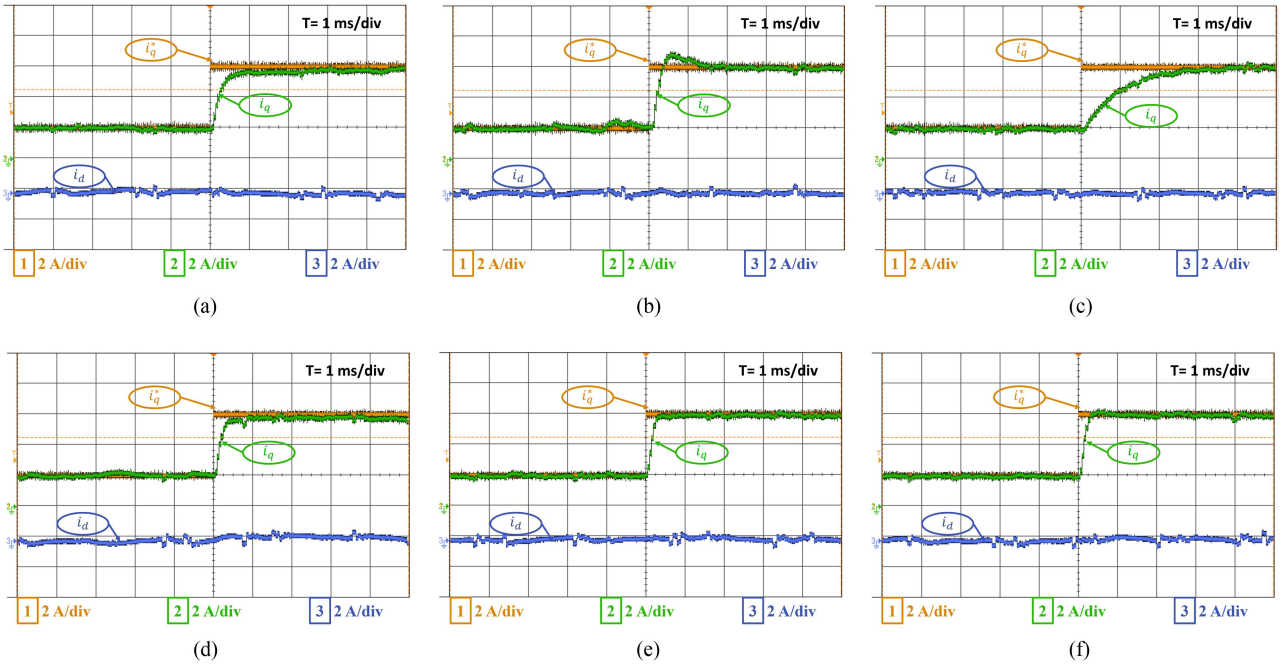

FIGURE 7. Regulating and tracking responses of the currents i_d and i_q, respectively, for different Current-loop controllers: (a) PI-1, (b) PI-2, (c) PIDO with $k_d = 1000$, (d) RCPI, (e) RDPI (at $\omega_g^* = 1000$ rpm), and (f) RDPI (at $\omega_g^* = 1200$ rpm).

incorporates two more PI controllers than the other methods. All the four PI controller gains are also listed in the table.

C. PERFORMANCES OF CURRENT-LOOP CONTROLLERS

The overall system dynamics include speed control, which involves a slower mechanical speed response. To assess the performance of the faster current control, experiments are performed only with the current controllers (open outer-loop speed control) and applying step changes to the reference current i_q^*. At an operating speed of $\omega_g = 1200$ rpm, i_q^* is changed from 2 to 6 A.

Fig. 7(a) and (b) shows the current responses for the conventional PI controllers. For the PI-1, shown in Fig. 7(a), the results are obtained for $\omega_{cc} = 2333$ with $\Delta = 0.9$. Additional values of ω_{cc} are also tested. Following the design philosophy, lower values of ω_{cc} result in slower responses. PI-1 exhibits a rise time of 1.1 ms and a settling time of 2.4 ms, with relatively higher steady-state current ripples.

For the PI-2, shown in Fig. 7(b), response alike a second-order system satisfying the damping ratio criterion is obtained. However, control saturation is observed due to the large integral gain. PI-2 achieves a shorter rise time of 0.3 ms and a settling time of 1.1 ms, with an overshoot of approximately 10%. The steady-state current ripple is comparable to that of PI-1.

The responses for the PIDO controller, with a desired settling time of $t_s = 4$ ms, are shown in Fig. 7(c). While the controller meets the desired settling time with lesser current ripple, choosing a smaller settling time results in higher observer gain, causing control saturation, which is exacerbated when a smaller settling time is chosen. As the PI gains are further increased (see Table 1), control saturation is observed.

TABLE 2. Performance Comparison of the Designed Controllers

Control	Rise time (ms)	Settling time (ms)	Overshoot (%)	Ripple i_q (A)	Ripple i_d (A)
PI-1	1.1	2.4	0	±0.4	±0.4
PI-2	0.3	1.1	10	±0.5	±0.4
PI-DO	1.8	3.5	0	±0.24	±0.3
RCPI	1.2	2.5	0	±0.5	±0.4
RDPI	0.25	0.9	3	±0.3	±0.3

The RCPI controller response, shown in Fig. 7(d), has a longer settling time, with larger oscillations in the steady-state due to the interactions of the two loops through the cross-control gains as well.

The RDPI controller, shown in Fig. 7(e), achieves better transient and steady-state performances with a more simpler control structure than the RCPI controller. Furthermore, when tested at a different speed of $\omega_g = 1000$ rpm, the RDPI controller exhibits robust performance similar to its performance at $\omega_g = 1200$ rpm, as shown in Fig. 7(f). The controller achieves shorter rise and settling times with smaller overshoot (less than 5%) and lesser steady-state current ripples. A comprehensive listing of the above-mentioned performances is given in Table 2.

For RCPI and RDPI, the regions between the dotted lines indicate the spread between their minimum and maximum singular values, capturing the effect of channel interactions (see Fig. 8(a)).

At low frequencies ($< 10^3$ rad/s), all controllers achieve effective disturbance rejection, with PI-2 being the most aggressive due to its higher integral gain, although this comes at the cost of greater high-frequency noise sensitivity. The

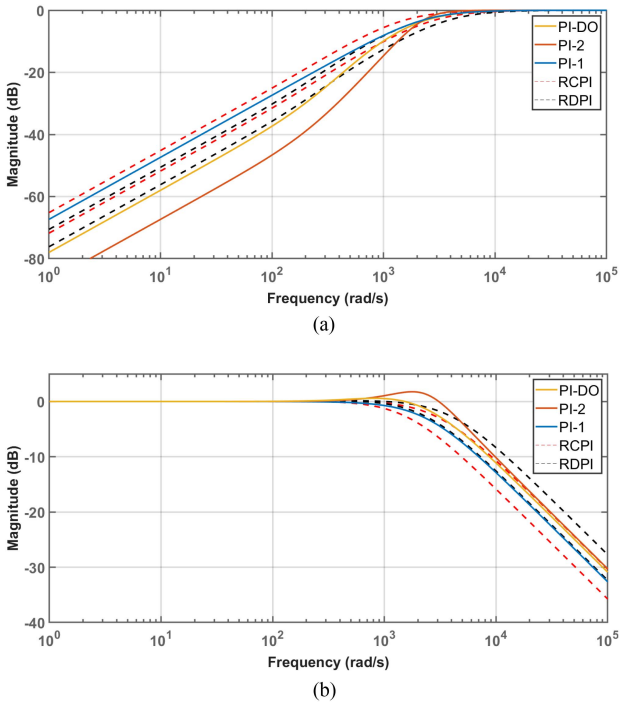

FIGURE 8. Singular value plots for different controllers. (a) Sensitivity function. (b) Complementary sensitivity function. For the MIMO controllers RCPI and RDPI, both the minimum and maximum singular values are shown.

peak in the complementary sensitivity plot for PI-2 indicates the response to be lesser damped, which is also observed in the corresponding responses, as shown in Fig. 8(b). At higher frequencies ($> 10^4$ rad/s), RCPI exhibits a sharp decline in sensitivity, improving disturbance rejection but raising concerns about robustness and noise amplification, as reflected in its complementary sensitivity response. RDPI maintains a more balanced profile across frequencies, it avoids the sharp roll-off of RCPI and excessive noise sensitivity of PI-2, thereby providing a more practical tradeoff between performance and robustness.

D. DESIGN AND PERFORMANCE OF SPEED-LOOP CONTROLLER

1) RDPI CONTROLLER DESIGN

Once the current controllers are designed, the known control gains are incorporated into the system dynamics, and the speed control problem is formulated, as discussed in Section III-B. The weight functions (see Fig. 4) are selected as

$$W_e = \frac{\omega_{lc}}{s + \omega_{lc}}, \quad W_u = 1, \quad W_t = \frac{s}{s + \omega_{hc}}$$

where the low-pass and high-pass filter parameters are set to $\omega_{lc} = 10$ and $\omega_{hc} = 1000$ [4]. The parameters for regional pole placement (see Fig. 5) are selected as $\alpha = 0.05$ (much slower than $\alpha = 100$ for the current-loop) and $\phi = 70^\circ$ for the outer speed loop. These values ensure that the speed dynamics are slower than the current loop, maintaining the cascade

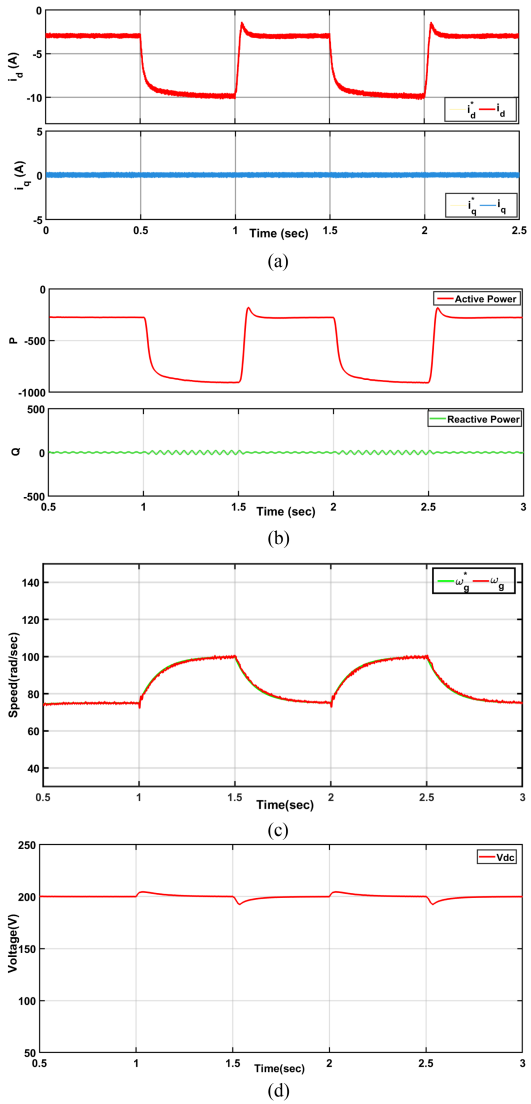

FIGURE 9. Responses with respect to change in speed reference ω_g^*. (a) Grid current i_{dg} and i_{qg}. (b) Active and reactive power fed to the grid. (c) Speed of pmsg. (d) Dc-link voltage.

control structure. The speed loop is less damped than the inner current loop due to the higher inertia of the wind turbine. The resulting controller gains are $k_{p\omega} = 0.18$ and $k_{i\omega} = 2.53$.

Fig. 10(a) illustrates the in-phase relationship between the grid voltage and current, confirming unity power factor operation. A zoomed-in view of the grid voltage and current waveforms in Fig. 10(b) further confirms this phase alignment.

2) PERFORMANCE OF SPEED CONTROLLER

Experiments are performed to assess the performance of the speed controller under varying wind speeds. The constant power mode was implemented, where the reference power to the dc machine emulating a wind turbine is generated based on wind power characteristics [2]. The reference speed ω_g^* for

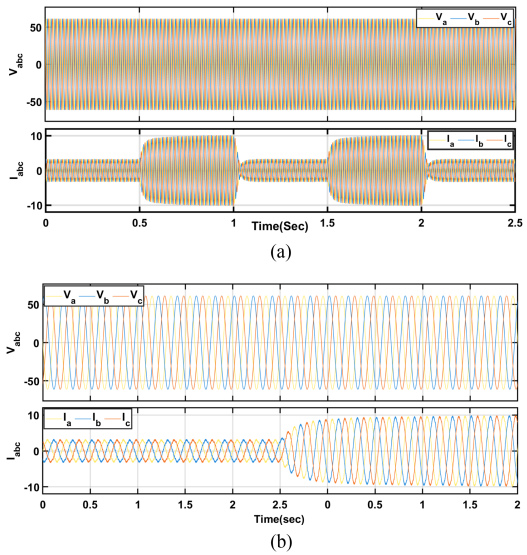

FIGURE 10. Responses with respect to change in speed reference ω_g^*. (a) Three-phase grid voltage (v_{abc}) and current (i_{abc}) fed to the grid. (b) Zoomed view of grid voltage and current.

the PMSG is

$$\omega_g^* = \frac{\lambda_{\text{opt}}}{R_b} v_w$$

where λ_{opt} and C_p are the optimal tip speed ratio and power coefficient, respectively, used to extract maximum power from the wind.

At a wind speed of 8 m/s, the rotor speed of the PMSG initially stabilizes at 750 rpm. When the wind speed increases from 8 to 10 m/s, the reference rotor speed (ω_g^*) is adjusted to 1000 rpm, and when the wind speed decreases back to 8 m/s, the reference speed follows accordingly. Figs. 9(a)–(d) depict the system's response to these step changes.

Fig. 9(a) illustrates the tracking behavior of the grid currents (i_d and i_q) in response to the wind speed variations. The quadrature-axis current (i_d) adjusts to regulate the power delivered to the grid, while the direct-axis current (i_q) ensures appropriate reactive power control. Negative power values indicate power injection into the grid. At $t = 0.5$ s and $t = 1.5$ s, when the wind speed increases, i_d changes from -3 to -9.8 A. Conversely, at $t = 1$ s and $t = 2$ s, when the wind speed decreases, i_d returns from -9.8 to -3 A.

Fig. 9(b) illustrates the active and reactive power fed to the grid. The active power increases in response to the wind speed change, demonstrating efficient power injection and utilization, while the reactive power is maintained around zero. Fig. 9(c) presents the rotor speed response of the PMSG, which accurately follows the reference speed, demonstrating the effectiveness of the speed-loop controller. Finally, Fig. 9(d) depicts the dc-link voltage response. The voltage remains well-regulated despite the change in wind speed, indicating effective control of the GSC.

These results validate the robust transient and steady-state performances of the proposed controllers in transferring power to the grid while adapting to wind-speed variations.

V. CONCLUSION

The design of PI controllers with a decentralized current-loop control structure in a robust control design framework for grid-connected PMSG is presented. The design follows two steps: 1) first, current controllers are designed in the MIMO framework, and 2) then, the speed controller is designed. A guideline (works as initial choices) for the weight functions for such robust controllers is provided. Since such structured controllers are to be designed using SOF design methods, a more straightforward LMI condition is provided for the current-loop controller design. In contrast, the speed controller is designed using the existing LMI criterion of [28]. The effectiveness of the designed controllers is demonstrated through experiments carried out on a 5 HP pmsg setup and performance comparison with other PI controller design methods is made.

Although improved performance is attained, there are many future scopes of the present work. The design is made based on the linearized dynamics at an operating point of speed. A further robust design that can incorporate uncertainties in the model due to the speed and other parameter variations could be investigated. Also, there are further scopes to fine-tune the weight selection for the controller design and optimize the choice of the scalar variables (see last paragraph of Section III-C) in the design criterion.

REFERENCES

[1] R. Pena, J. Clare, and G. Asher, "Doubly fed induction generator using back-to-back PWM converters and its application to variable-speed wind-energy generation," *IEE Proc.-Electric Power Appl.*, vol. 143, no. 3, pp. 231–241, 1996.

[2] A. Bakbak, H. T. Canseven, M. Ayaz, M. Altintaş, and E. Meş e, "Maximizing energy extraction from direct grid coupled PMSG for wind energy conversion systems," *IEEE Trans. Ind. Appl.*, vol. 58, no. 3, pp. 3888–3900, May/Jun. 2022.

[3] L. Fan, *Control and Dynamics in Power Systems and Microgrids*. Boca Raton, FL, USA: CRC Press, 2017.

[4] S. Das and B. Subudhi, "A H_∞ robust active and reactive power control scheme for a PMSG-based wind energy conversion system," *IEEE Trans. Energy Convers.*, vol. 33, no. 3, pp. 980–990, Sep. 2018.

[5] M. A. A. Murad and F. Milano, "Modeling and simulation of PI-controllers limiters for the dynamic analysis of VSC-based devices," *IEEE Trans. Power Syst.*, vol. 34, no. 5, pp. 3921–3930, Sep. 2019.

[6] M. A. A. Murad, M. Liu, and F. Milano, "Modeling and simulation of variable limits on conditional anti-windup PI controllers for VSC-based devices," *IEEE Trans. Circuits Syst. I: Reg. Papers*, vol. 68, no. 7, pp. 3079–3088, Jul. 2021.

[7] W. Ho, O. Gan, E. Tay, and E. Ang, "Performance and gain and phase margins of well-known PID tuning formulas," *IEEE Trans. Control Syst. Technol.*, vol. 4, no. 4, pp. 473–477, Jul. 1996.

[8] M. Chinchilla, S. Arnaltes, and J. Burgos, "Control of permanent-magnet generators applied to variable-speed wind-energy systems connected to the grid," *IEEE Trans. Energy Convers.*, vol. 21, no. 1, pp. 130–135, Mar. 2006.

[9] Y.-C. Kwon, S. Kim, and S.-K. Sul, "Voltage feedback current control scheme for improved transient performance of permanent magnet synchronous machine drives," *IEEE Trans. Ind. Electron.*, vol. 59, no. 9, pp. 3373–3382, Sep. 2012.

[10] S.-K. Kim, J.-S. Lee, and K.-B. Lee, "Offset-free robust adaptive back-stepping speed control for uncertain permanent magnet synchronous motor," *IEEE Trans. Power Electron.*, vol. 31, no. 10, pp. 7065–7076, Oct. 2016.

[11] S.-K. Kim, K.-G. Lee, and K.-B. Lee, "Singularity-free adaptive speed tracking control for uncertain permanent magnet synchronous motor," *IEEE Trans. Power Electron.*, vol. 31, no. 2, pp. 1692–1701, Feb. 2016.

[12] W. Guo and D. Liu, "Adaptive neural network command filtered backstepping control for the underactuated TORA system," *IEEE Access*, vol. 11, pp. 13679–13689, 2023.
[13] J. Ansari, M. Homayounzade, and A. R. Abbasi, "Innovative load frequency control: Integrating adaptive backstepping and disturbance observers," *IEEE Access*, vol. 13, pp. 53673–53693, 2025.
[14] K. Koiwa, Y. Li, K.-Z. Liu, T. Zanma, and J. Tamura, "Full converter control for variable-speed wind turbines without integral controller or PLL," *IEEE Trans. Ind. Electron.*, vol. 67, no. 11, pp. 9418–9428, Nov. 2020.
[15] Y. He et al., "Direct predictive voltage control for grid-connected permanent magnet synchronous generator system," *IEEE Trans. Ind. Electron.*, vol. 70, no. 11, pp. 10860–10870, Nov. 2023.
[16] T. Thomas, M. K. Mishra, C. Kumar, and M. Liserre, "Control of a PV-wind based DC microgrid with hybrid energy storage system using Lyapunov approach and sliding mode control," *IEEE Trans. Ind. Appl.*, vol. 60, no. 2, pp. 3746–3758, Mar./Apr. 2024.
[17] C. Wei, J. Xu, Q. Chen, C. Song, and W. Qiao, "Full-order sliding-mode current control of permanent magnet synchronous generator with disturbance rejection," *IEEE J. Emerg. Sel. Topics Ind. Electron.*, vol. 4, no. 1, pp. 128–136, Jan. 2023.
[18] P. Chen and Y. Luo, "Analytical fractional-order PID controller design with Bode's ideal cutoff filter for PMSM speed servo system," *IEEE Trans. Ind. Electron.*, vol. 70, no. 2, pp. 1783–1793, Feb. 2023.
[19] Y. Belkhier, S. Fredj, H. Rashid, and M. Benbouzid, "Robust nonlinear control of permanent magnet synchronous motor drives: An evolutionary algorithm optimized passivity-based control approach with a high-order sliding mode observer," *Eng. Appl. Artif. Intell.*, vol. 145, 2025, Art. no. 110256.
[20] Y. Belkhier and A. Oubelaid, "Passivity-based control of PMSM servo system with load torque adaptation: Theoretical and experimental validation," *IEEE Trans. Transport. Electrific.*, vol. 11, no. 1, pp. 4494–4503, Feb. 2025.
[21] R. Errouissi and A. Al-Durra, "A novel PI-type sliding surface for PMSG-based wind turbine with improved transient performance," *IEEE Trans. Energy Convers.*, vol. 33, no. 2, pp. 834–844, Jun. 2018.
[22] R. Krishnan, *Permanent Magnet Synchronous and Brushless DC Motor Drives*. Boca Raton, CA, USA: CRC Press, 2017.
[23] S. Skogestad and I. Postlethwaite, *Multivariable Feedback Control: Analysis and Design*. England, U.K.: Wiley, 2005.
[24] M. Taherzadeh, M. A. Hamida, M. Ghanes, and M. Koteich, "A new torque observation technique for a PMSM considering unknown magnetic conditions," *IEEE Trans. Ind. Electron.*, vol. 68, no. 3, pp. 1961–1971, Mar. 2021, doi: 10.1109/TIE.2020.2972429.
[25] M. Chilali and P. Gahinet, "H_∞ design with pole placement constraints: An LMI approach," *IEEE Trans. Autom. Control*, vol. 41, no. 3, pp. 358–367, Mar. 1996.
[26] M. Chilali, P. Gahinet, and C. W. Scherer, "Multi-objective output-feedback control via LMI optimization," *IFAC Proc. Volumes*, vol. 29, pp. 1691–1696, 1996.
[27] V. Blondel and J. N. Tsitsiklis, "NP-hardness of some linear control design problems," *SIAM J. Control Optim.*, vol. 35, no. 6, pp. 2118–2127, 1997.
[28] P. R. Sahoo, J. K. Goyal, S. Ghosh, and A. K. Naskar, "New results on restricted static output feedback controller design with regional pole placement," *IET Control Theory Appl.*, vol. 13, no. 8, pp. 1095–1104, 2019.
[29] S. Boyd, L. El Ghaoui, E. Feron, and V. Balakrishnan, *Linear Matrix Inequalities in System and Control Theory*. Philadelphia, PA, USA: Soc. Ind. Appl. Math., 1994.
[30] S. Tolani, S. Joshi, and P. Sensarma, "Dual-loop digital control of a three-phase power supply unit with reduced sensor count," *IEEE Trans. Ind. Appl.*, vol. 54, no. 1, pp. 367–375, Jan./Feb. 2018.
[31] X. Wang, C. Jiang, F. Zhuang, C. H. T. Lee, and C. C. Chan, "A harmonic injection method equivalent to the resonant controller for speed ripple reduction of PMSM," *IEEE Trans. Ind. Electron.*, vol. 69, no. 10, pp. 9793–9803, Oct. 2022.
[32] L. Wang, S. Chai, D. Yoo, L. Gan, and K. Ng, *PID and Predictive Control of Electrical Drives and Power Converters Using MATLAB/Simulink*. Hoboken, NJ, USA: Wiley, 2015.
[33] R. Errouissi, A. Al-Durra, and M. Debouza, "A novel design of PI current controller for PMSG-based wind turbine considering transient performance specifications and control saturation," *IEEE Trans. Ind. Electron.*, vol. 65, no. 11, pp. 8624–8634, Nov. 2018.

ADITYA KUMAR (Student Member, IEEE) received the B.Tech. degree in electronics and instrumentation engineering from Bharath University, Chennai, India, in 2011, and the M.Tech. degree in control and automation from the National Institute of Technology, Rourkela, India, in 2014. He is currently working toward the Ph.D. degree in control systems with the Indian Institute of Technology (BHU), Varanasi, India.

He is a Researcher with Control Systems Laboratory, BHU. His research interests include advanced control strategies for power converters, renewable energy systems, and electrical drives.

SHIV PRAKASH received the bachelor's degree in electrical engineering from Dr. A.P.J. Abdul Kalam Technical University, Lucknow, India, in 2017, and the master's degree in electrical machines and drives from the Indian Institute of Technology (BHU), Varanasi, India, in 2021. He is currently working toward the Ph.D. degree in power electronics and control with Control Systems Laboratory, BHU.

His research interests include battery management systems and power electronic converters for electric vehicle applications.

SANDIP GHOSH (Member, IEEE) received the B.Eng. degree in electrical engineering from the Indian Institute of Engineering Science and Technology, Shibpur, India, in 1999, the master's degree in control system engineering from Jadavpur University, Kolkata, India, in 2003, and the Ph.D. degree from Indian Institute of Technology, Kharagpur, India, in 2010.

He was with Electrical Engineering Department, National Institute of Technology, Rourkela, India, and was a Postdoctoral Fellow with the University of Cape Town, Cape Town, South Africa. He is currently with the Department of Electrical Engineering, Indian Institute of Technology, Banaras Hindu University, Varanasi, India. His research interests include robust control design and its applications.

N. K. SWAMI NAIDU received the B.Tech. degree in electrical and electronics engineering from Jawaharlal Nehru Technological University, Hyderabad, India, in 2007, the M.Tech. degree in power electronics and drives from the National Institute of Technology, Kurukshetra, India, in 2009, and the Ph.D. degree in electrical machine drives from the Department of Electrical Engineering, Indian Institute of Technology, New Delhi, India, in 2015.

He was a Postdoctoral Research Fellow with Nanyang Technological University, Singapore. He is currently an Assistant Professor with the Department of Electrical Engineering, Indian Institute of Technology, Varanasi, India. His research interests include power electronics, WECSs, power quality improvement, and microgrid-based power systems.

PAWEL DWORAK (Senior Member, IEEE) received the M.Sc., Ph.D., and D.Sc. degrees in control engineering from the West Pomeranian University of Technology in Szczecin, Poland, in 1999, 2005, and 2016, respectively.

He is currently an Associate Professor with the West Pomeranian University of Technology, Szczecin, Poland. His research interests include multivariable control systems, adaptive control, optimal control, and industrial applications of modern control algorithms.